The Journal of Immunology

Imaging of Cell–Cell Communication in a Vertical Orientation Reveals High-Resolution Structure of Immunological Synapse and Novel PD-1 Dynamics

Joon Hee Jang, Yu Huang, Peilin Zheng, Myeong Chan Jo, Grant Bertolet, Michael Xi Zhu, Lidong Qin and Dongfang Liu

J Immunol 2015; 195:1320-1330; Prepublished online 29 June 2015;
doi: 10.4049/jimmunol.1403143
http://www.jimmunol.org/content/195/3/1320

The Journal of Immunology is published twice each month by
The American Association of Immunologists, Inc.,
1451 Rockville Pike, Suite 650, Rockville, MD 20852

Print ISSN: 0022-1767 Online ISSN: 1550-6606.

Imaging of Cell–Cell Communication in a Vertical Orientation Reveals High-Resolution Structure of Immunological Synapse and Novel PD-1 Dynamics

Joon Hee Jang,*,† Yu Huang,†,‡ Peilin Zheng,† Myeong Chan Jo,* Grant Bertolet,†,§ Michael Xi Zhu,‡ Lidong Qin,*,¶ and Dongfang Liu†,§

The immunological synapse (IS) is one of the most pivotal communication strategies in immune cells. Understanding the molecular basis of the IS provides critical information regarding how immune cells mount an effective immune response. Fluorescence microscopy provides a fundamental tool to study the IS. However, current imaging techniques for studying the IS cannot sufficiently achieve high resolution in real cell–cell conjugates. In this study, we present a new device that allows for high-resolution imaging of the IS with conventional confocal microscopy in a high-throughput manner. Combining micropits and single-cell trap arrays, we have developed a new microfluidic platform that allows visualization of the IS in vertically "stacked" cells. Using this vertical cell pairing (VCP) system, we investigated the dynamics of the inhibitory synapse mediated by an inhibitory receptor, programed death protein-1, and the cytotoxic synapse at the single-cell level. In addition to the technique innovation, we have demonstrated novel biological findings by this VCP device, including novel distribution of F-actin and cytolytic granules at the IS, programed death protein-1 microclusters at the NK IS, and kinetics of cytotoxicity. We propose that this high-throughput, cost-effective, easy-to-use VCP system, along with conventional imaging techniques, can be used to address a number of significant biological questions in a variety of disciplines. ***The Journal of Immunology*****, 2015, 195: 1320–1330.**

The ability of cells to communicate with each other is one of the most essential and fundamental activities in eukaryotic organisms. The cells of the immune system communicate with each other through a variety of strategies. One of the most important of these is the formation of an interface structure known as the immunological synapse (IS) (1–6). Since its original description (5), an enormous body of evidence has been accumulated showing that the IS plays a pivotal role in the immune response, mediating such vital functions as immune recognition, adhesion, activation, and inhibition (2, 7, 8).

Given the critical role of the IS in immune responses against cancer and infection, it is essential to understand the molecular mechanisms underlying IS formation, signaling, and function in real cell–cell conjugates. Conventional confocal microscopy of both fixed and live cells represents the most common imaging technique to study the IS in most research laboratories. Traditionally, immune cells are mixed with target cells or APCs. After fixation, cell–cell conjugates are imaged under a confocal microscope. However, current methods of imaging the synapse face several limitations. One of the most obvious of these is the low resolution of IS images in lateral cell–cell conjugates. Because virtually all conjugates lie parallel to the plane of focus, the synaptic interface lies perpendicular to the plane of focus, along the *z*-axis (see Fig. 1A, *left*). This requires that sequential z-stacked images be taken to capture the entire synapse. However, because conventional confocal microscopes typically have poor resolution along the *z*-axis (9, 10), it is challenging to obtain high-resolution synapse images (see Fig. 1A).

In this geometry, the resolution at the synapse is greatly reduced due to the elongated point spread function of the incident laser beam (see Fig. 1A, *right*) (9, 10). The resolution can be improved by simply rotating the cell pair, positioning the IS on a horizontal imaging plane (see Fig. 1B). Recently, to achieve an ideal focal plane for IS imaging, researchers manually oriented the cells on top of one another using optical tweezers (11, 12). This technique was able to successfully enhance the resolution in which the synapse could be visualized. However, it was still subject to a few major challenges, such as significant phototoxicity and low frequency of cell–cell conjugates.

To further circumvent these obstacles, the combination of total internal reflection fluorescence (TIRF) microscopy with the glass-supported planar lipid bilayer (SLB) is currently used to study IS

*Department of Nanomedicine, Houston Methodist Research Institute, Houston, TX 77030; †Center for Human Immunobiology, Texas Children's Hospital, Department of Pediatrics, Baylor College of Medicine, Houston, TX 77030; ‡Department of Integrative Biology and Pharmacology, Graduate Program in Cell and Regulatory Biology, University of Texas Health Science Center at Houston, Houston, TX 77030; §Department of Pathology and Immunology, Baylor College of Medicine, Houston, TX 77030; and ¶Department of Cell and Developmental Biology, Weill Cornell Medical College, New York, NY 10065

Received for publication December 19, 2014. Accepted for publication May 23, 2015.

This work was supported by National Institutes of Health/National Institute on Drug Abuse Grant 1R01DA035868-01 and Cancer Prevention and Research Institute of Texas Grant CPRIT-R1007. This work was also supported in part by Baylor–University of Texas Houston Center for AIDS Research Core Support Grant AI36211 from the National Institute of Allergy and Infectious Diseases, Caroline Wiess Law Fund for Research in Molecular Medicine Grant 2531319101, Texas Children's Hospital Pediatric Pilot Research Fund Grant 2531319301, and by the Lymphoma Specialized Programs of Research Excellence Developmental Research Program from Baylor College of Medicine and Methodist Research Institute Grants 2531319302 and P50CA126752.

Address correspondence and reprint requests to Dr. Lidong Qin or Dr. Dongfang Liu, Department of Nanomedicine, Houston Methodist Research Institute, 6670 Bertner Avenue, Houston, TX 77030 (L.Q.) or Center for Human Immunobiology, Texas Children's Hospital, Department of Pediatrics, Baylor College of Medicine, 1102 Bates Street, Suite 330, Houston, TX 77030 (D.L.). E-mail addresses: LQin@tmhs.org (L.Q.) or dongfang.liu@bcm.edu (D.L.)

The online version of this article contains supplemental material.

Abbreviations used in this article: 2D, two-dimensional; 3D, three-dimensional; D→C→D, "dispersed→centralized→dispersed"; FWHM, full width at half maximum; HEK, human embryonic kidney; IS, immunological synapse; PD-1, programmed death protein-1; PD-L1, programmed death protein ligand 1; PDMS, polydimethylsiloxane; sD, "stay dispersed"; SLB, glass-supported planar lipid bilayer; TIRF, total internal reflection fluorescence; VCP, vertical cell pairing.

formation, signaling, and function (13–16). Although this hybrid technique certainly improves the resolution due to the horizontal interface between immune cells and their artificial APCs or target cells, TIRF illumination is restricted to within 100–200 nm from the coverslip (17). Another potential limitation of this system is that the SLB does not adequately mimic the complex surface of a target cell (2, 8, 16, 18, 19), thus giving rise to potentially nonphysiological features in the resulting IS. Furthermore, researchers must deal with lateral movement of live cells during live cell imaging, which causes cells of interest in the imaging chamber to often drift out of the field of view. When cell density is low, random cell movements significantly reduce the chance of finding stable cell–SLB interaction under each imaging field. This makes it time-consuming to find a stable synapse under this circumstance. Alternatively, when loading cells at higher densities, the cells often form large clusters that make it difficult to observe individual cell–SLB interactions. Additionally, both TIRF and optical tweezers are costly and labor-intensive. Successful operation of each system requires extensive training.

Recently, a micropit system has been developed to achieve high-resolution IS imaging between effector and target cells at low cost (20). However, the loading efficiency of cells in the micropit system alone is low (~10–15%). Meanwhile, the frequency of vertical orientation stacking between effector and target cells is also relatively low, which makes imaging time-consuming. Therefore, development of a novel system would fill a significant unmet need to study IS formation and cell–cell communication.

In this study, we have developed a novel system to study the IS horizontally in a high-resolution and high-throughput manner. Combining micropits with single-cell trap arrays, this newly developed microfluidic platform provides various technical novelties that answer the previously discussed difficulties in IS imaging. The vertical cell orientation enables imaging the IS in a horizontal plane and enhances resolution on both fixed and live cell imaging. This vertical cell pairing (VCP) system can minimize the lateral cell drift at the focal plane and constrain the conjugated cells in the vertical position. This system can also capture >3000 conjugates at a time with high loading efficiency. Using this VCP system, we present a "face-to-face" look at the structure of the human NK cell IS. Compared to conventional cell–cell conjugates, the organization of F-actin at the IS can be clearly observed at the VCP system with high resolution using conventional confocal microscopy. Our system was able to detect the positioning of perforin-positive lytic granules over regions of low F-actin density at the IS, a detail that has been previously reported under superresolution microscopy (21, 22), but one that has proven difficult to image using conventional approaches. Additionally, bright F-actin puncta that were segregated from the cytolytic granules were observed at the center of the NK synapse, which is usually indiscernible with conventional confocal microscopy. Furthermore, the novel dynamics of programmed death protein-1 (PD-1) microclusters at the NK synapse and target cell lysis mediated by NK cells at a real cell–cell interface were also observed in the VCP system. Thus, our VCP system provides a high-throughput, high-efficiency, and user-friendly approach to IS imaging that not only successfully addresses many of the problems of previous techniques, but also possesses broad potential applications in a variety of other biological disciplines.

Materials and Methods

Microfluidic device fabrication

The schematic flow of the fabrication procedure is summarized in Supplemental Fig. 1. Negative photoresist (SU-8 3025, MicroChem, Newton, MA) was coated on an oxygen plasma–cleaned silicon(100) wafer (500 μm thickness, Silicon Quest International, San Jose, CA). The spin coater (WS-400BZ, Laurell Technologies, North Wales, PA) was set at 500 rpm for 10 s to evenly spread the photoresist on the wafer. The resist was spun at 2900 rpm for 30 s, yielding a 30-μm thickness for the top mold, and at 4000 rpm for 60 s, yielding a 15-μm thickness for the bottom mold. The resist was soft baked for 3 min at 95°C and exposed to UV light through the photomask. After baking the resist at 65°C for 1 min and 95°C for 4 min and developing, the micropit and trap array molds were obtained. The mold was coated with trimethylchlorosilane at atmospheric pressure for 30 min. An overall design of the photomask to produce the mold is shown in a Supplemental Fig. 2A and 2B.

Polydimethylsiloxane (PDMS, Sylgard 184, Dow Corning) was mixed with curing agent at a ratio of 10:1. The micropit array mold (bottom mold) was dipped into the PDMS and pressed on a number 1.5 cover glass (170 μm thickness) with 40 Newtons by a heated mechanical press (CH4386, Carver). The PDMS was cured at 80°C for 2 h, and the mold was removed to obtain the bottom layer. The PDMS was poured onto the trap array mold (top mold) and cured at 77°C for 1 h. The PDMS was lifted from the mold to obtain the top layer. The inlet hole (4 mm diameter) and negative pressure port (0.5 mm diameter) were punched (Accu-Punch, Syneo) into the top PDMS layer. A drop of methanol was applied for lubrication and the top layer was snapped on the bottom layer to assemble the two layers.

Cell culture

The K562 myelogenous leukemia cell line (American Type Culture Collection) was cultured in RPMI 1640 medium (Life Technologies, Carlsbad, CA). The KHYG-1 human NK cell line (23), expressing CD16 (CD16-KHYG-1), was maintained in R10 medium consisting of RPMI 1640 medium (Life Technologies) supplemented with 10% FBS (Life Technologies), 10 mM HEPES (Life Technologies), 1 mM sodium pyruvate (Cellgro, Manassas, VA), 2 mM L-glutamine (Life Technologies), and 1% MEM nonessential amino acids solution (Life Technologies). Additionally, 1 μg/ml cyclosporin A (Sigma-Aldrich, St. Louis, MO), 50 μg/ml Primocin, and 10 U/ml IL-2 were freshly added into the R10 medium for each passage. The culture medium for CD16-KHYG-1 cells was replaced with cyclosporin A–free medium 1 d before use. The human embryonic kidney (HEK)293T cells were cultured in DMEM (Life Technologies) with 10% FBS, 10 mM HEPES, and 2 mM L-glutamine.

Plasmids and transduction of CD16–KHYG-1 and K562 cell lines

To generate the PD-1–GFP construct, the full length of the PD-1–GFP fusion protein sequence (OriGene Technologies, Rockville, MD) was amplified by the primers 5′-AATCCGGAATTCGCCGCCGCGATCGCCATGC-3′ (forward) and 5′-AATCGCGGATCCTTAAACTCTTTCTTCACC-3′ (reverse). The PCR product digested with EcoRI and BamHI (Thermo Scientific) was ligated with EcoRI- and BamHI-digested lentivector pCDH (24). Similarly, to generate the C-terminal mCherry-tagged PD ligand 1 (PD-L1) construct, the PD-L1 cDNA (OriGene) was amplified by the primers 5′-AATCCGGAATTCATGAGGATATTTGCTGTCT-3′ (forward) and 5′-AATCGCGGATCCCGTCTCCTCCAAATGTGTA-3′ (reverse). The PCR product was digested with EcoRI and BamHI and ligated with an mCherry-N1 vector (Clontech) to generate C-terminal mCherry-tagged PD-L1. The sequence of PD-L1–mCherry was then amplified by the primers 5′-TAGAGCTAGCGAATTATGAGGATATTTGCTGTCTTTA-3′ (forward) and 5′-ATTTAAATTCGAATTTCACGCCTTGTACAGCTCGTCC-3′ (reverse). The PCR product was inserted into EcoRI digested pCDH lentivector by the In-Fusion cloning system (Clontech). All plasmids were verified by sequencing.

To generate the PD-1–GFP$^+$ CD16–KHYG-1 and PD-L1–mCherry$^+$ K652 cell lines, both CD16–KHYG-1 and K562 cell lines were transduced with the pCDH cDNA cloning and expression lentivirus system (System Biosciences), respectively. The lentivirus was generated by cotransfecting HEK293T cells with a lentiviral vector containing PD-1–GFP or PD-L1–mCherry and three packaging plasmids (pMLg/pRRE, pRSV-Rev, pMD2.g) by Lipofectamine reagent (Invitrogen). Briefly, 0.8 μg total DNA (0.128 μg pCDH, 0.32 μg pMLg/pRRE, 0.16 μg pRSV-Rev, 0.192 μg pMD2.g) was mixed with 4 μl Lipofectamine and added into one well of HEK293T cells cultured in a six-well plate with ~90% confluence. Viral particles were harvested and filtered by a 0.45-μm filter (GE Healthcare) after 48 h transfection. Then, 2×10^5 CD16–KHYG-1 or K562 cells suspended in 4 ml R10 medium were infected with 4 ml viral supernatant. Transduced cells were cultured for 24 h in the presence of 8 μg/ml Polybrene and subsequently sorted by a FACSAria II cell sorter (BD Biosciences). The expression of PD-1–GFP and PD-L1–mCherry were verified by flow cytometry (BD LSRFortessa).

Cell loading

The fabricated VCP microfluidic device was placed on a vacuum desiccator for 15 min. A 1-ml syringe was connected to the port through a tube to generate negative pressure and a drop of 2% BSA in PBS was introduced into the inlet. The device was incubated for 30 min at 37˚C. Then, R10 medium was subsequently used to replace the BSA solution in the device. Ten microliters of the first cell suspension with a concentration range of 10^6–10^7 cells/ml was added into the inlet. The flow rate of 15 μl/min was used to seed the cells using a syringe pump. After 30 s of seeding, the rest of the cell suspension was washed three times with PBS. The microfluidic device was disconnected from the syringe and centrifuged (Sorvall Legend X1R, Thermo Scientific) at 2000 rpm (700 × *g*) for 10 min to spin down the cells into micropit array. After centrifugation, the syringe was reconnected and the second cell suspension was added into the inlet. The parameters for seeding the second cell suspension were the same as those for the first cell suspension.

For live cell imaging, we first injected the K562 cells stably expressing PD-L1–mCherry into the device. The device was mounted on the inverted fluorescence microscope stage. A single cell was focused upon with a ×63 oil immersion objective lens. Then, the CD16–KHYG-1 cells expressing PD-1–GFP were injected. After the effector cells were anchored on top of the target cells, the cell suspension in the inlet was replaced with fresh cell medium containing 25 mM HEPES buffer. Live cell imaging was performed at the synapse plane every 30 s for 10 min. During the live cell imaging, the flow rate was maintained at 0.5 μl/min.

For fixed cell imaging, the CD16–KHYG-1 cells were injected first. The device was incubated for 1 h at 37˚C. The cell–cell conjugates were fixed by 4% formaldehyde solution in PBS for 15 min, then washed with PBS for 5 min. Permeabilization buffer containing 5% of normal donkey serum and 0.5% Triton X-100 in PBS was added into the device. The device was incubated in 4˚C overnight. The permeabilization buffer was washed with PBS for 5 min. Then, primary Ab against α-tubulin (Abcam) in Ab buffer containing 3% normal donkey serum and 0.5% Triton X-100 in PBS was pumped into the device. The device was incubated at 4˚C overnight. The Ab buffer was washed with PBS for 5 min. The cells were stained by fluorescently labeled secondary Ab (Life Technologies). The Ab buffer was washed with PBS for 5 min, and, finally, a drop of ProLong Gold antifade reagent mounting medium (Life Technologies) was added into the device.

Confocal microscope

High-resolution images were captured with a confocal fluorescence microscope (Leica TCS SP8, Leica Microsystems) equipped with a ×63 oil immersion objective lens (1.47 numerical aperture, Leica Microsystems). In the fixed cell images, z-stacks of tubulin, perforin, and actin were sequentially captured. The high-resolution live cell images were carried out at 37˚C. The 4.5-μm z-stacks centered at the IS were acquired to account for movement within the live cell. The fluorescence from PD-1–GFP, PD-L1–mCherry, and the bright field image was detected simultaneously. The images were acquired by LAS AF software (Leica) and analyzed with ImageJ and Imaris (Bitplane) software.

Table I. Previous and current version of vertical cell pairing device developed in this work

	Micropit	Microtrap	VCP ver.1	VCP ver.2	VCP ver.3
Design	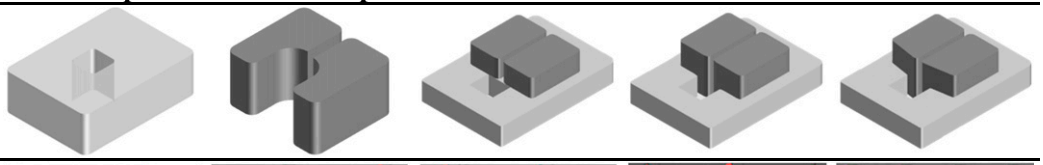				
Cell loading	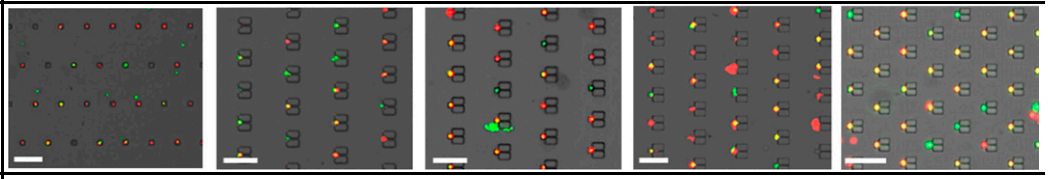				
Efficiency	~30 %	~30 %	~55%	~55%	~70%
Disadvantage	Cells are paired by random motion. There is no cell movement restriction. Multiple cells in the pit	Cells are paired by random chance. Multiple cells in the trap	Multiple cells in the trap Difficult and labor intensive for aligning two layers	Multiple cells in the trap	Not noted
Improvement		Movement of trapped cell pairs is restricted by microfluidic force.	Two layer system provides better pairing efficiency.	Top layer can be snapped into bottom layer. The snap-in structure provides easy alignment.	10° of sweep angle is added. Most of trapped cells form 1 to 1 conjugates with improved efficiency.

Results

Design optimization of VCP microfluidic device

The development and optimization process of the VCP device design is summarized in Table I. We previously tested a single-layer micropit and microtrap design, from which ~30% of heterogeneous cell pairs was achievable with optimized loading conditions (Table I). By combining the micropit with a micropillar, the pairing efficiency increased to ~55% (VCP version 1). However, aligning the two layers in microscale was time-consuming and labor-intensive. Furthermore, it was nearly impossible to align the whole area perfectly due to PDMS shrinkage during the curing process. Thus, we designed the device with a snap-in structure (VCP version 2). The two layers were aligned by snapping the trap structures of the top layer together with the through-holes of the bottom layer by one-click alignment, where the micropits of the bottom layer line up with the microtraps of the top layer (Supplemental Fig. 1). This method can achieve precise alignment of all microstructures without the need for any specialized tools (25–28). This method also prevents alignment shift problems and PDMS shrinkage ratio mismatches that occur in the previous two-layer design (29, 30). The 15-μm height of the micropit array is overlaid with the 30-μm height of the microtrap array, creating a 15-μm-high flow channel between the two PDMS layers. Further optimization of the design was made by adding a sweep angle to the micropillar (VCP version 3). The 10° sweep angle on the micropillar provides better one-on-one cell pairs with improved loading efficiency of >70%. Detailed dimensions of the device are shown in Supplemental Fig. 2.

The fabrication method is described in greater detail in *Materials and Methods*. Briefly, a PDMS prepolymer–coated mold of the bottom layer, which contains 4000 individual micropits, was directly stamped onto a No. 1.5, 170-μm-thick cover glass. The top layer, which includes the microtrap array, was prepared by standard photolithography procedures (31–33).

The microfluidic device features four areas, including inlet, negative pressure port, zone 1, and zone 2 to control the flow rate and direction (Fig. 1C). Media and cell suspensions were injected via the inlet. Flow pressure is generated by a 1-ml syringe connected to the negative pressure port. Zone 1 consists of microchannels to break up the cell clusters and evenly distribute the flow of medium and suspended cells into zone 2. Zone 2 contains the microtrap array, which captures the cells. There are two pathways for governing the cell loading mechanism (Fig. 1C). The horizontal pathway flows (labeled as pathways 1 and 2, respectively) around the microtrap structure and passes through a 3-μm gap between traps. Once the cell suspension is injected via the inlet, the cell preferentially takes pathway 1 owing to the high flow rate. When multiple cells are taking the same pathway, the flow is disturbed, and a single cell can be anchored in between the trap by taking pathway 2. Once a cell is wedged into the 3-μm gap between the trap, the flow distribution around the trap is changed due to the blockage by the trapped cell. Thus, the subsequent cells take pathway 1, leaving a single cell trapped in the microstructure, which constrains lateral cell movement. Detailed flow velocity distributions are simulated in Fig. 2. The low-flow velocity area in Fig. 2B is extended after trapping a cell between the micropillars, which contributes to reduce flow resistance (Fig. 2C). Thus, subsequent cells preferentially bypass the micropillars. Of note, the previous study shows that the cavity under the laminar flow does not affect overall flow characteristics, whereas the laminar flow might introduce vortex in the cavity (34, 35). Therefore, we omitted the microtrap structures to demonstrate the flow distribution.

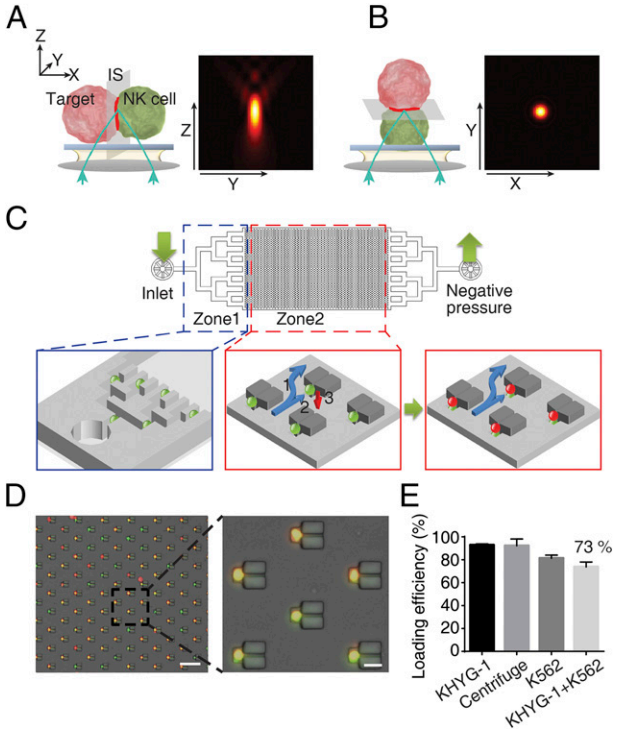

FIGURE 1. Optical geometry and device design. (**A**) The optical geometry (*left*) for imaging the IS by conventional methods and corresponding simulated point spread function (*right*) of the excitation beam. (**B**) The optical geometry (*left*) for imaging the IS by the VCP system and corresponding simulated point spread function (*right*) of the excitation beam. (**C**) Overall design of the microfluidic platform and flow pathways during cell loading. VCP version 3 is shown. (**D**) Wide-field fluorescent microscopic image merged with bright field image of the microfluidic device after cell loading. Red and green channels correspond to K562 and KHYG-1 cells, respectively. Scale bar, 100 μm (*left*) and 20 μm (*right*). (**E**) Percentage of trap-captured cells in each step during the cell loading procedure. The graph shows average and SD of cell capture efficiency over four different areas of the device. The results are from three independent experiments.

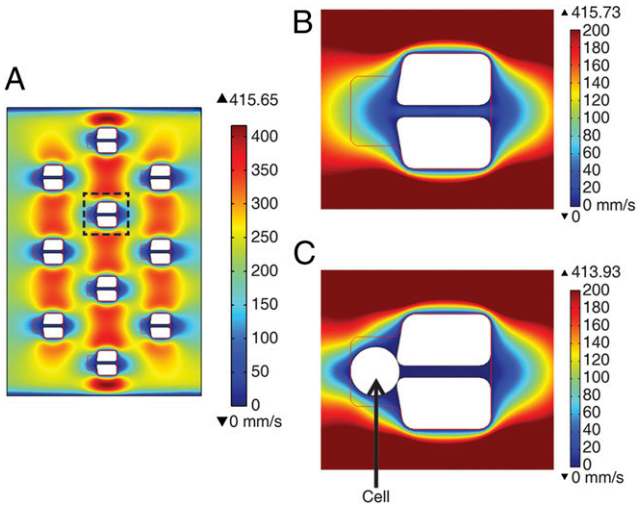

FIGURE 2. Simulated flow velocity distribution on the top layer. (**A**) Overview of the flow velocity in VCP version 3. (**B**) Flow velocity distribution around a single microstructure without cell. Red lines show bottom layer and white blocks indicate top PDMS structure. (**C**) Flow velocity distribution changes around a single microstructure with a trapped cell. The flow velocity is pseudo-colored with cool and warm colors indicating low and high flow velocity, respectively.

The gravitational force (red arrow in Fig. 1C) pulling the cell down into the micropit is negligible in this system. The micropit is initially filled with cell suspension medium. The approximate density of the medium is 1.0 g/ml, according to the manufacturer, and that of the blood cell is 1.1 g/ml (36). Thus, the horizontal flow pinning the cell against the microtrap easily overwhelms the gravitational force acting on the cell. However, artificially increasing the gravitational force by centrifugation readily brings the cell down into the micropit. After this, the second cell suspension was injected and anchored on top of the first cells by the same mechanism (Fig. 1C, 1D).

To test the loading efficiency of the device, the fraction of the captured cells in each step was measured as shown in Fig. 1. First, an NK cell line, CD16–KHYG-1 (green in Fig. 1D), was injected into the device with 92.8 ± 1.1% trapping efficiency. The percentage of the captured cells was maintained at 92.2 ± 5.9% after centrifugation. The sequential injection of target K562 cells (a human immortalized myelogenous leukemia line; red in Fig. 1D) achieved a capture efficiency of 81.3 ± 2.7%. Finally, the percentage of the microstructures trapping both KHYG-1 and K562 cells was 73.7 ± 4.4% (Fig. 1E). Independently, we assessed the factors that affect loading efficiency such as flow rate and cell loading density. For the flow rate, we used 15 μl/min for cell loading and 0.5 μl/min for live cell imaging to minimize shear stress on cells. The loading efficiency increased as a function of cell loading density (Supplemental Fig. 1B, 1C). Throughout the experiment, we used ~10^6 cells suspended in 50 μl medium and were able to image the cell pairs with 60–70% efficiency. These results demonstrate that we can successfully fabricate a device that is capable of cocapturing vertically "stacked" target and effector cells in a high-throughput, high-efficiency manner.

High-resolution imaging intracellular structure of the IS on fixed cells by the VCP system

After successfully developing this device, we further tested whether it would permit high-resolution imaging with a conventional confocal microscope, a common instrument in most of research institutes. We used the CD16–KHYG-1 cells as effector cells and the K562 cell line as susceptible target. The CD16–KHYG-1 effector cells were loaded into the device, followed by the target cells. After fixation, cell–cell conjugates were stained for F-actin, perforin, and tubulin. As a control, conventional microscopy slides were prepared simultaneously, as previously described (13, 15, 37). Three-dimensional (3D) images were acquired in each fluorescence channel. After reconstruction of the 3D stack, a z-projection of the interface between two cells was presented (Fig. 3).

The representative image obtained by the VCP device demonstrates significant improvements over that of the image obtained by the conventional method in two respects. First, our system prevents deformation of the IS. In the traditional method, cells spread out

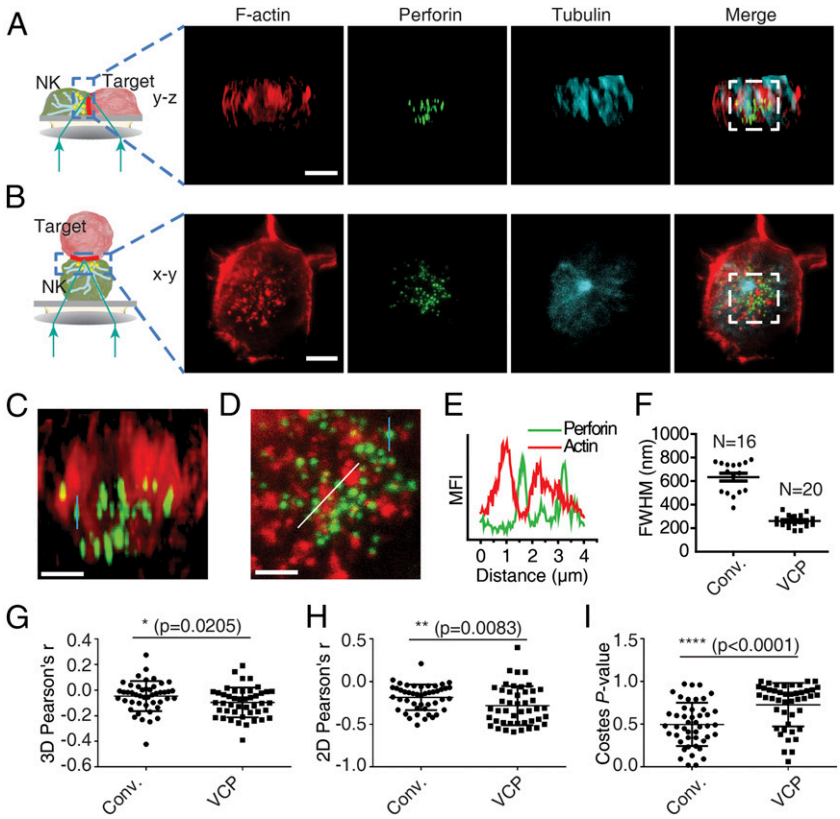

FIGURE 3. Comparison of IS structure by conventional (Conv.) and VCP systems imaged by confocal fluorescence microscopy. CD16–KHYG-1 (NK) cell conjugated with K562 (target) cell on cover glass coated with poly-L-lysine (**A**) and vertical stack of NK target cell pair by VCP version 2 (**B**) are fixed, permeabilized, and stained for F-actin (red), perforin (green), and α-tubulin (cyan). Scale bars, 5 μm. The 3D fluorescent images centered at the IS are z-projected. Magnified areas (8 × 8 μm, white boxes) from the fluorescent microscope image obtained by using coverslips coated with poly-L-lysine (**C**) and by using the VCP version 2 system (**D**). Perforin (green) and F-actin (red) are visualized. Scale bars, 2 μm. (**E**) Fluorescence intensity profiles of F-actin and perforin were measured across the white line. Fluorescence intensities of perforin and F-actin are shown in the green and red lines, respectively. (**F**) FWHM and SE of fluorescence intensity for individual perforin granule along the vertical line [blue line in (C) and (D)]. (**G**) Pearson correlation coefficient (r) was calculated for perforin and F-actin from 3D colocalization analysis. Each dot represents each pair (n = 46 for conventional, n = 45 for VCP imaging). (**H**) Pearson correlation coefficient (r) was calculated from two-dimensional (2D) colocalization analysis. The same set of data as (G) was used. (**I**) Costes p value (indicating the reliability of Pearson correlation coefficient analysis) obtained during 2D colocalization analysis. VCP version 3 was used for (G)–(I).

due to the interaction between the plasma membrane and the polylysine-coated coverslip (Fig. 3A, Supplemental Video 1). In contrast, the VCP system maintained the IS in its natural shape without distortion (Fig. 3B, Supplemental Video 2). Second, the VCP device provides superior spatial resolution compared with the conventional method. A zoomed-in area taken from the 3D confocal images acquired by both the conventional coverslips (Fig. 3C) and VCP device (Fig. 3D) was compared. The round shape of perforin-positive cytolytic granules was easily distinguished in the image measured by the VCP device, whereas the cytolytic granules appeared elongated in the image achieved by the conventional method. Furthermore, the detail of the fine F-actin meshwork in the image obtained by the VCP device (Fig. 3D) was greater than that of the image acquired by the conventional approach (Supplemental Videos 1 and 2). Perforin-positive cytolytic granules were observed positioned over low-density areas of F-actin (Fig. 3E), in agreement with previous observations (11, 21, 22, 38). To quantify the improvement in resolution, we measured the full width at half maximum (FWHM, an indicator of the granule size) of the fluorescence line intensity profiles of the cytolytic granules. The FWHM of the cytolytic granules measured with the VCP device was significantly smaller than that of those measured using the conventional approach (Fig. 4E).

To further quantify the unique features of F-actin puncta that appear well segregated from the perforin-positive cytolytic granules in the IS, we carried out colocalization analysis and calculated a Pearson correlation coefficient (Pearson *r*) for the images obtained using the VCP system and the conventional method (Fig. 3, Supplemental Fig. 3). F-actin formed numerous puncta at the center of the IS, where the perforin-positive cytolytic granules were well segregated by these F-actin puncta (a phenomenon that could not be appreciated in the side view using the conventional method), which is distinct from the previous observations that F-actin is cleared at the center of synapse (39–43). To further quantify these observations, we calculated the Pearson *r* from 3D and two-dimensional (2D) colocalization analysis by Imaris (Bitplane)

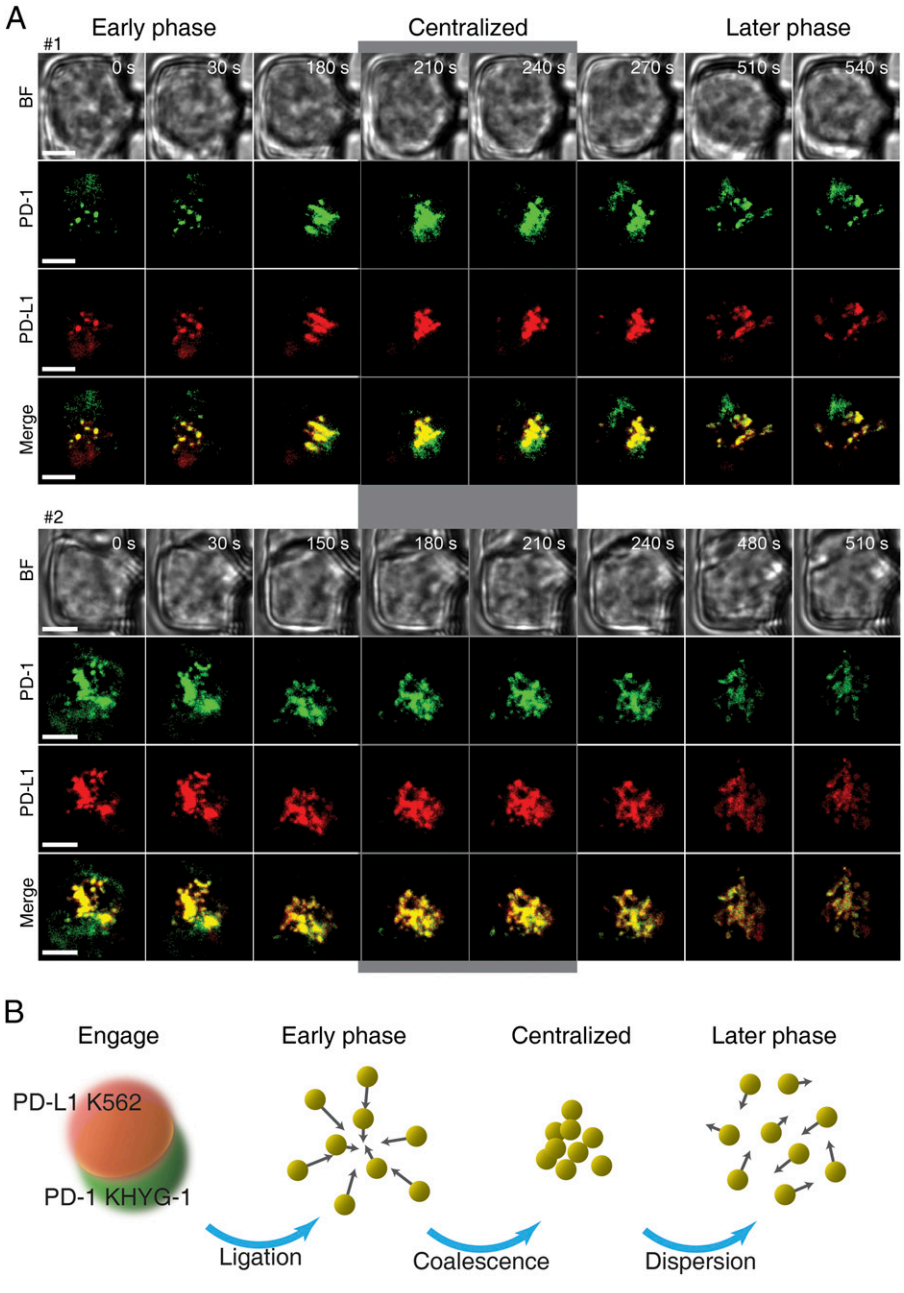

FIGURE 4. Time-lapse images of "dispersed→centralized→dispersed" (D→C→D) PD-1/PD-L1 clusters by 3D confocal fluorescence microscope using VCP version 3. (**A**) Two examples of a subpopulation of NK/target cell pairs (68.2%, 15 of 22 observations) whose PD-1/PD-L1 microclusters coalesced, then dispersed. Scale bars, 5 μm. (**B**) Proposed model of PD-1/PD-L1 cluster movement during cell–cell communication within the D→C→D subpopulation.

and ImageJ software, respectively (Fig 3G, 3H). A striking negative correlation between perforin and F-actin at the NK cell synapse has been observed by using both conventional and new VCP imaging methods. To quantitatively determine which method provides a more reliable set of analysis, we extracted a Costes *p* value (44) from two-dimensional colocalization analysis (Fig 3I). Whereas the conventional method shows an average of 50% confidence level, most of the *p* values obtained by the VCP system show confidence levels close 100%. Taken together, these results demonstrate that the resolution with which the IS can be visualized in the VCP system is superior to that of conventional methods.

High-resolution imaging of dynamics of PD-1 microclusters on live cells by the VCP system

Live imaging provides unprecedented information on the dynamics of the inhibitory IS (13), which cannot be obtained from images of fixed cells. After successfully demonstrating the high-resolution imaging of the IS made possible by the VCP system, we further tested whether this device allows live-cell imaging of the IS. In this study, we used fluorescently tagged PD-1, an important inhibitory receptor expressed on lymphocytes, as a mode to study the dynamics of the inhibitory synapse. To test whether we could use this VCP system to visualize the dynamics of PD-1 at the IS, we used CD16-KHYG-1 cells expressing PD-1-GFP together with susceptible K562 target cells expressing PD-L1–mCherry (Supplemental Fig. 4). Live cell imaging revealed that PD-1 and PD-L1 microclusters formed three distinct patterns at the NK IS. To further quantify the three different patterns, we imaged 22 live cell pairs independently (Figs. 4–6, Supplemental Videos 3, 4). To capture the early phase of IS formation, PD-1–GFP$^+$ CD-16 KHYG-1 cells were loaded into the VCP device first. After mounting the VCP device on the microscope, the PD-L1–mCherry$^+$ K652 target cells were added into the VCP device. We categorized the 22 cell pairs into three different patterns based on the movement of PD-1 microcusters at the NK IS (Supplemental Video 3). Most conjugates (68.2%, 15 of 22) showed that the PD-1/PD-L1 clusters coalesce in the center of the IS at the early phase (<5 min after interaction) and then disperse into the periphery of the IS in the later phase (Fig. 4). We termed this dynamic PD-1/PD-L1 movement in the synapse "dispersed→centralized→dispersed" (D→C→D), as shown in Fig. 4. Given that this pattern was observed in the most conjugates (68.2%), we propose a model of the dynamic movement of PD-1/PD-L1 clusters (Fig. 4B) in which PD-1/PD-L1 microclusters coalesced to the center of IS in the early phase of IS formation (within 1–2 min). Then, these temporally centralized clusters dissociate from each other and disperse within the entire synapse with random movement.

We also observed a second pattern of PD-1/PD-L1 microcluster movement within the synapse, in which PD-1/PD-L1 does not form a centralized cluster during the 10-min time-lapsed imaging acquisition (Fig. 5, Supplemental Video 3). These PD-1/PD-L1 microclusters (22.7%, 5 of 22 conjugates) remain dispersed during the acquisition (Fig. 5). We named this pattern as "stay dispersed" (sD), as shown in Fig. 5.

In addition to the D→C→D and sD patterns, we also observed that a small minority of PD-1/PD-L1 microclusters (9.1%, 2 of 22 conjugates) form at the periphery of the IS and coalesce at the

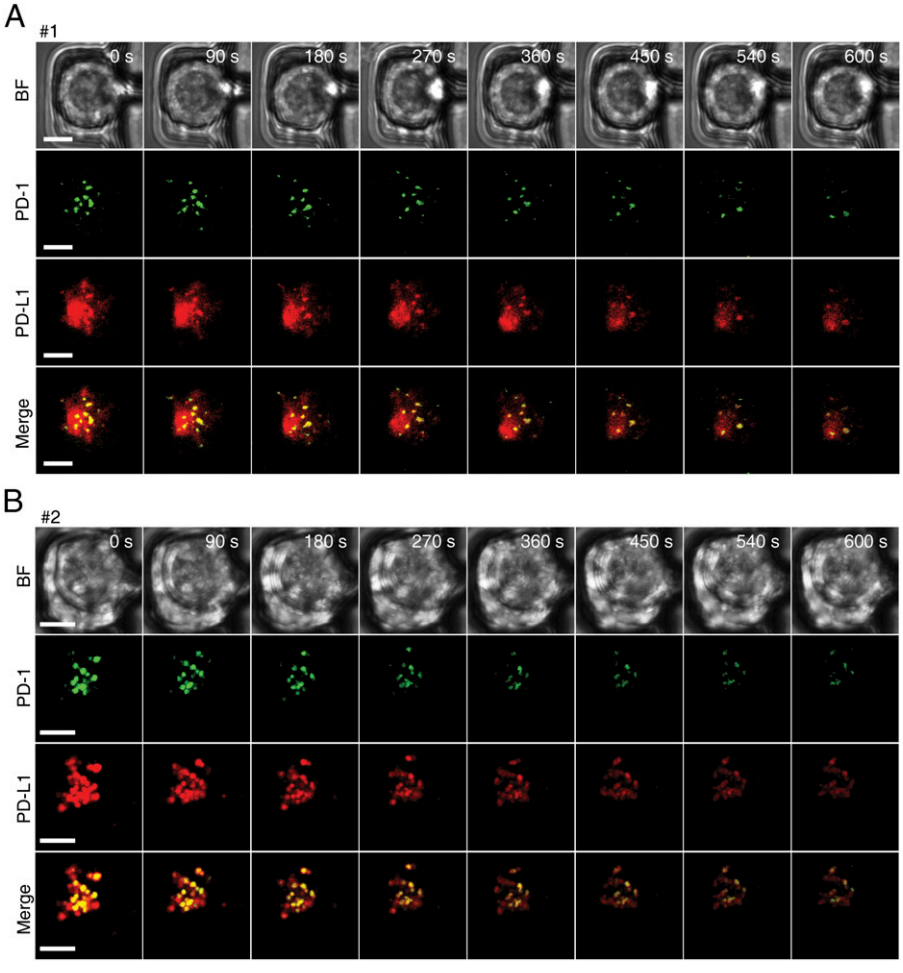

FIGURE 5. Time-lapse images of "stay dispersed" (sD) PD-1/PD-L1 clusters by 3D confocal fluorescence microscope. (**A**) and (**B**) represent two examples of a subpopulation of PD-1/PD-L1 cluster movement on two cell pairs imaged using VCP version 3. During imaging, the clusters did not coalesce in this subpopulation (22.7%, 5 of 22 observations). Scale bars, 5 μm.

center of the synapse, where they remain clustered (Fig. 6A, Supplemental Videos 3, 4). We named this dynamic of PD-1/PD-L1 movement in the synapse "dispersed→stay centralized." Consistent with previous observations (13), PD-1 microclusters were similar to HLA-E clusters that formed between SLBs and human primary NK cells. To quantify the temporal dynamics of PD-1 and PD-L1 microclusters, we tracked the trajectory of individual microclusters over time. As shown in Fig. 6B, nine microclusters accumulated rapidly at the center of synapse. The average velocity of each trajectory was calculated (19 ± 5 nm/s, $n = 9$). To confirm stable inhibitory synapse formation on vertically oriented NK and K562 cells in the VCP system, we continuously flowed medium during imaging, with a constant flow rate of 0.5 μl/min. Once the flow was removed after experiment, the CD16–KHYG-1 cell being imaged (green, *top*) was released from the top layer of the single cell trap, but remained anchored to the top of the K562 cell (red, *bottom*; (Fig. 6C).

From these observations, we conclude that the dynamics of inhibitory synapse microclusters in live cells can be readily observed in the VCP system. To our knowledge, this is the first observation of single microcluster dynamics at the IS in a real cell–cell conjugate with high resolution. Meanwhile, the distinct patterns of PD-1/PD-L1 microclusters in the IS are a striking feature of inhibitory synapses formed between PD-1$^+$ NK cells and PD-L1$^+$ target cells.

Kinetics of live NK cell cytotoxicity detected by the VCP system

We next sought to test whether cytolytic killing could be monitored by the VCP system in live cells. To test this, K562 cells were loaded with calcein AM green viability dye (45–47). To distinguish the effectors from the target cells, CD16–KHYG-1 cells were labeled with CellTracker red (48). Cell–cell conjugates were imaged by wide-field fluorescence microscopy (Fig. 7, Supplemental Movies 5, 6). The disappearance of calcein AM green fluorescence signal was used as a readout for effective killing of target cells. A clear decrease in the green fluorescent signal was observed in the K562 cells cocultured with CD16–KHYG-1 effector cells (Fig. 7A, Supplemental Video 5). A relatively stable red signal and a sudden decrease in green signal were observed in one cell–cell conjugate (Supplemental Video 6). To quantify the kinetics of cytotoxicity in the VCP system, 204 effector/target cell pairs were analyzed. The fluorescence intensity from K562 cells labeled with calcein AM green were measured every 10 min (Fig. 7B). The kinetics of cytotoxicity elicited by NK cells was categorized by the fluorescence intensity profile of K562 cells. In this study, we used the complete disappearance of calcein AM as a readout for cell death. Around 45.6% of K562 cells (93 of 204 conjugates) still fluoresced after 6 h conjugation with NK cells, suggesting that these K562 cells remained alive (Fig. 7C). We named this fluorescence profile "slow decay." The average fluorescence decay profile of K562 cells was comparable to that of unconjugated K562 cells (green line in Fig. 7B).

In addition to the slow decay fluorescence profile from calcein AM green, we also observed three different kinetics of disappearance of calcein AM green in K562 cells. The second pattern of calcein AM (33.8%, 69 of 204 conjugates) displayed a "single drop" profile, indicating lysis of K562 cells by NK cells (Fig. 7D). Consistent with previous observations (49, 50), the average time for NK-mediated cytotoxicity was ~222.2 min (SD of 84.3 min) after injection (Fig. 7D).

The third fluorescence profile of calcein AM (11.3%, 23 of 204 conjugates) was termed "fast decay" (Fig. 7E). In the fast decay dynamic, the level of calcein AM green eventually became undetectable within 6 h after conjugation, suggesting a different cytotoxicity mechanism elicited by NK cells (49, 50).

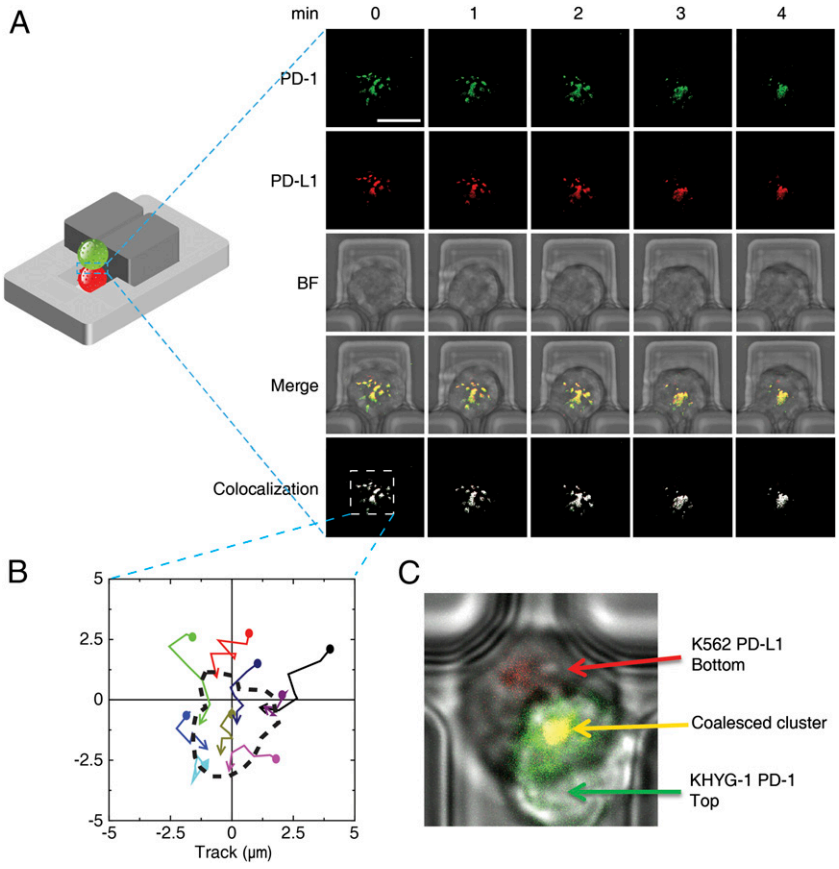

FIGURE 6. Time-lapse images of "dispersed→stay centralized" PD-1/PD-L1 clusters (9.1%, 2 of 22 observations) by 3D confocal fluorescence microscope. (**A**) Schematic model (*left*) and time series taken from Supplemental Video 3 (*right*). Fluorescent images of selected time points from live cell imaging by using the VCP version 2 system for IS formation between PD-L1–mCherry$^+$ K562 (*bottom*, red) and PD-1–GFP$^+$ CD16-KHYG-1 (*top*, green) cells. PD-1–GFP, PD-L1–mCherry, bright field, merged, and colocalization of PD-1 and PD-L1 are presented. Scale bar, 10 μm. (**B**) Track path of the clusters in the colocalized fluorescence image. Black dashed line indicates central cluster region. (**C**) Fluorescent image merged with bright field image after disconnecting negative pressure.

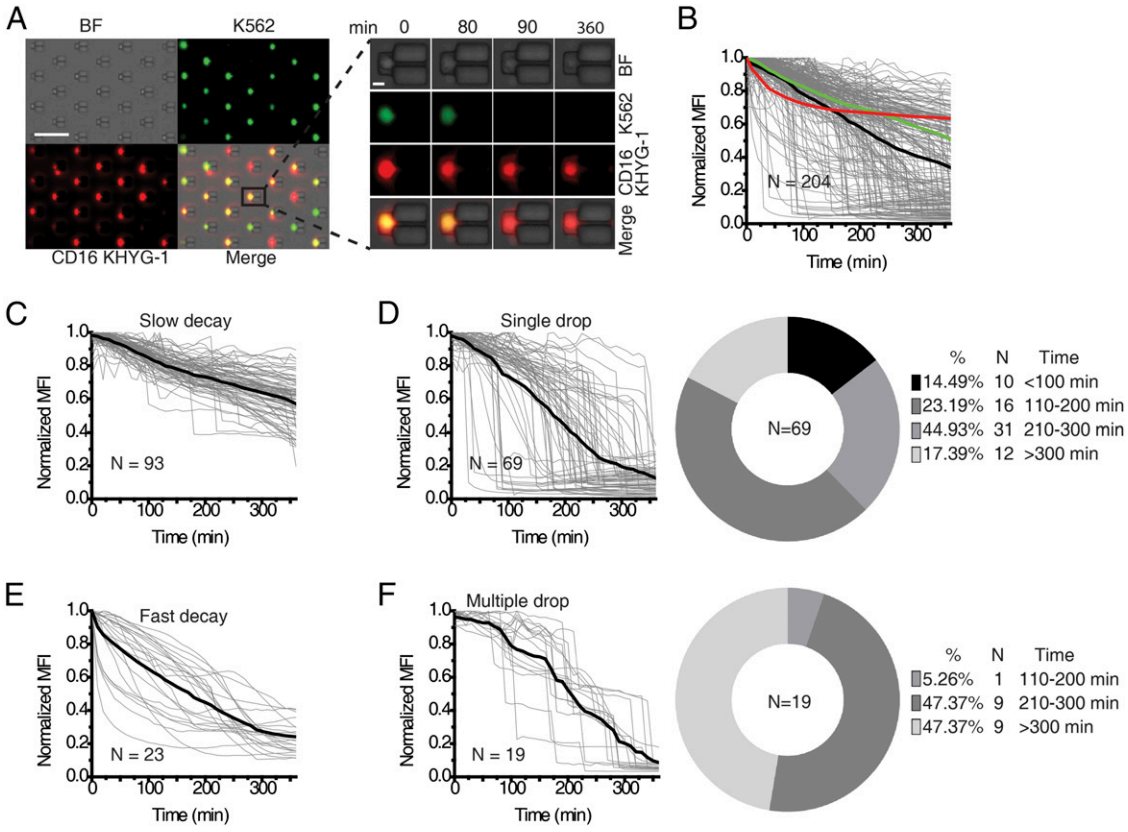

FIGURE 7. Kinetics of cytotoxicity mediated by NK cells imaged under wide-field fluorescence microscope. (**A**) Live cell time-lapse images from the VCP version 3 system used to establish kinetics of CD16–KHYG-1 (red)-mediated cytotoxicity against K562 (green) target cell. Scale bars, 100 μm (*left*) and 10 μm (*right*), respectively. (**B**) Mean fluorescent intensity (MFI) of K562 cells paired with CD16–KHYG-1 cells (gray), K562 cells alone (green), and CD16–KHYG-1 cells alone (red) during the 6 h acquisition. (**C**–**F**) Classification of killing kinetics of NK cells when paired with K562 target cells. (C) Slow decay of normalized MFI from K562 cells conjugated with NK cells for 6 h. (D) Single drop of normalized MFI from K562 cells conjugated with NK cells (*left*) and quantification of single drop occurrence in K562 cells after conjugation with NK cells (*right*). (E) Fast decay of normalized MFI from K562 cells conjugated with NK cells for 6 h. (F) Multiple drop of normalized MFI from K562 cells conjugated with NK cells (*left*) and quantification of multiple drop occurrence in K562 cells after conjugation with NK cells (*right*). Black lines indicate average of each population.

Notably, multiple stepwise decreases over time (multiple drop profile) in calcein AM fluorescence (9.3%, 19 of 204 conjugates) were also observed (Fig. 7F), suggesting a potential mechanism with multiple cytolytic hits from NK cells (51). Average cell death time in this subpopulation was determined to be 293.2 min (SD of 49.1 min).

Altogether, these data show that the kinetics of cytotoxicity over time can be readily detected by the VCP system in both a high-throughput manner and at the single-cell level, refinements that are all lost by conventional 4 h Cr^{51}-release assays, which only provide a blanket measure of killing activity over the entire culture after a certain time period, and are incapable of distinguishing between individual cytolytic and noncytolytic cell pairings.

Discussion

The IS is a critical platform for mediating an effective immune response in both the adaptive and innate immune systems (2, 52). Current research on synaptic geometry is restricted in artificial systems such as Ab-coated coverslips or SLB systems (13, 14, 21). In this study, we developed a high-throughput VCP microfluidic system to study the IS in an actual cell–cell communication setting. A detailed protocol for generating this system is provided in the present study. Using this system, a high-resolution image at the IS formed between and effector and target cell under conventional confocal microscopy has been achieved. Additionally, potential applications of this system have been demonstrated by investigating the dynamics of PD-1/PD-L1 microcluster formation at the IS, providing, to our knowledge, the first observation of microclusters at the IS in vertically oriented real cell–cell conjugates, as well as the kinetics of killing at the single-cell level. Our findings offer the scientific community a user-friendly VCP system and demonstrate the feasibility and application of this novel technique for studying cell–cell communications in a variety of disciplines. Additionally, by using this VCP system, we provide insights on several significant biological questions.

Compared to the micropit system developed by Biggs et al. (20), the VCP system possesses two distinct advantages. The rate of successful vertical conjugates is significantly higher in our system (~73% versus 10–15%) due to the novel combination of the micropit system with a single-cell trap array, which efficiently guides the cells into the pits. Second, our VCP system addresses one of the major difficulties of the original micropit system, wherein there was an unavoidable tradeoff between loading efficiency (i.e., success rate of two-cell pairs entering single pits) and vertical orientation. In the micropit system, a larger pit diameter allows for higher loading efficiency, but because of the large pericellular area of the micropit, the top cell will often not be perfectly aligned on top of the bottom one (20). Conversely, a narrower pit diameter significantly decreases the loading efficiency. By guiding the cells into narrow micropits by the single-cell trap array, our system is able to maintain a vertical orientation without compromising loading efficiency.

As a result of its innovative design, the VCP system has addressed a number of significant questions. The organization of F-actin at the cytotoxic IS is still highly controversial (53). In the T cell IS, it has been shown that F-actin is totally cleared from the center of synapse, which facilities degranulation events at the center of the IS (39–43). However, this phenomenon is different in the NK cell synapse. Using superresolution-stimulated emission depletion and structured illumination microscopy, two independent research groups have shown that F-actin is not totally cleared at the center of the IS (11, 21). Instead, a punctuated, low-density F-actin meshwork has been observed at the center of the NK cell synapse, where perforin-positive cytolytic granules are well segregated by the F-actin puncta. In agreement with these observations, perforin-positive cytolytic granules are seen positioned at low-density F-actin regions in our system, a crucial detail that is usually indiscernible with conventional confocal microscopy. Using this VCP system, to our knowledge for the first time, we observed clearly that perforin-positive cytolytic granules are located among low density F-actin regions in the center of the IS formed between NK and target cells, without the need for superresolution imaging techniques. Therefore, our results support the phenomenon that F-actin "hypodensities" are present at the center of the IS in human NK cells and that cytolytic granules converge at these hypodensities.

In addition to the information gained from fixed-cell imaging, live imaging with the VCP system provides additional, critical information on the dynamics of the inhibitory IS not available from previous studies of fixed NK cells. PD-1 is an emerging immune checkpoint protein highly upregulated in T, B, and NK cells in the setting of chronic viral infection and tumorigenesis (54, 55). Similar to other inhibitory receptors such as KIR and CD94/NKG2A, the intracellular domain of PD-1 contains an ITIM, which plays a critical role in NK cell inhibition (56). Engagement of PD-1 with PD-L1 inhibits cytotoxic killing of K562 target cells by CD16–KHYG-1 cells, which indicates the occurrence of an inhibitory synapse (Y. Huang and D. Liu, unpublished data). However, whether NK cells can form a stable inhibitory synapse is still controversial. Previous studies have shown that NK cells do not form stable synapses in the presence of inhibitory receptors (57, 58). Using the VCP platform, we observed that the microclusters of PD-1 and PD-L1 at the IS coalesce into a central cluster at the synapse. This pattern is reminiscent of previous studies that show that human primary NK cells form stable inhibitory synapse on lipid bilayers carrying HLA-E, a ligand for inhibitory receptor CD94/NKG2A (13). Meanwhile, our results obtained by this novel VCP system demonstrate three distinct PD-1/PD-L1 microcluster patterns at the NK IS, which to our knowledge is the first to describe the dynamics of PD-1 microclusters in a real cell–cell conjugate at high resolution without the need of an expensive superresolution imaging system.

An understanding of the forces that govern the stability of the IS is essential to identify its function. One of the most important functions of the IS is to mediate directed cytotoxicity toward target cells (59). Typical methods of monitoring NK cell cytotoxicity, such as Cr^{51}-release assays with obvious radiation safety implications, are expensive and time-consuming. The VCP platform developed in the present study allows rapid, quantitative, high-throughput functional measurements to monitor NK cell cytotoxicity in real time. The disappearance of the dye in the target cell within a single pit provides a clear readout for cell death at the single-cell level, unobscured by the presence of other effector/target pairs, which can be an issue in a large open-well system (49). Therefore, in addition to providing a platform for enhanced study of the IS, our system provides an alternate method for studying IS-mediated cellular cytotoxicity.

In conclusion, we have developed a novel, high-throughput VCP system to study cell–cell communications for both fixed and live cell imaging. The feasibility and potential application of this VCP system has been demonstrated in this study. We propose that this high-throughput and user-friendly VCP system offers a powerful new imaging platform that can be used to address a number of significant questions in immunology and cell biology, such as single-cell analysis, cell fusion, cell–cell communication, and cell surface ligand mobility.

Acknowledgments

We thank Dr. Emily Mace and Dr. Malini Mukherhee for help with microscopic imaging. We also thank Dr. Pinaki Banerjee for help with flow cytometry, Dr. David T. Evans (University of Wisconsin) for the CD16-KHYG-1 cell line, Dr. Jordan S. Orange (Baylor College of Medicine) for the K562 and HEK293T cell lines, and Dr. Guangwei Du (University of Texas Health Science Center at Houston) for the pCDH lentiviral vectors.

Disclosures

The authors have no financial conflicts of interest.

References

1. Bromley, S. K., W. R. Burack, K. G. Johnson, K. Somersalo, T. N. Sims, C. Sumen, M. M. Davis, A. S. Shaw, P. M. Allen, and M. L. Dustin. 2001. The immunological synapse. *Annu. Rev. Immunol.* 19: 375–396.
2. Davis, D. M., and M. L. Dustin. 2004. What is the importance of the immunological synapse? *Trends Immunol.* 25: 323–327.
3. Grakoui, A., S. K. Bromley, C. Sumen, M. M. Davis, A. S. Shaw, P. M. Allen, and M. L. Dustin. 1999. The immunological synapse: a molecular machine controlling T cell activation. *Science* 285: 221–227.
4. Davis, D. M., I. Chiu, M. Fassett, G. B. Cohen, O. Mandelboim, and J. L. Strominger. 1999. The human natural killer cell immune synapse. *Proc. Natl. Acad. Sci. USA* 96: 15062–15067.
5. Monks, C. R., B. A. Freiberg, H. Kupfer, N. Sciaky, and A. Kupfer. 1998. Three-dimensional segregation of supramolecular activation clusters in T cells. *Nature* 395: 82–86.
6. Monks, C. R., H. Kupfer, I. Tamir, A. Barlow, and A. Kupfer. 1997. Selective modulation of protein kinase C-θ during T-cell activation. *Nature* 385: 83–86.
7. Lee, K. H., A. D. Holdorf, M. L. Dustin, A. C. Chan, P. M. Allen, and A. S. Shaw. 2002. T cell receptor signaling precedes immunological synapse formation. *Science* 295: 1539–1542.
8. Dustin, M. L. 2014. What counts in the immunological synapse? *Mol. Cell* 54: 255–262.
9. Nasse, M. J., and J. C. Woehl. 2010. Realistic modeling of the illumination point spread function in confocal scanning optical microscopy. *J. Opt. Soc. Am. A Opt. Image Sci. Vis.* 27: 295–302.
10. Hell, S. W., S. Lindek, C. Cremer, and E. H. K. Stelzer. 1994. Measurement of the 4pi-confocal point spread function proves 75 nm axial resolution. *Appl. Phys. Lett.* 64: 1335.
11. Brown, A. C., S. Oddos, I. M. Dobbie, J. M. Alakoskela, R. M. Parton, P. Eissmann, M. A. Neil, C. Dunsby, P. M. French, I. Davis, and D. M. Davis. 2011. Remodelling of cortical actin where lytic granules dock at natural killer cell immune synapses revealed by super-resolution microscopy. *PLoS Biol.* 9: e1001152.
12. Oddos, S., C. Dunsby, M. A. Purbhoo, A. Chauveau, D. M. Owen, M. A. Neil, D. M. Davis, and P. M. French. 2008. High-speed high-resolution imaging of intercellular immune synapses using optical tweezers. *Biophys. J.* 95: L66–L68.
13. Liu, D., M. E. Peterson, and E. O. Long. 2012. The adaptor protein Crk controls activation and inhibition of natural killer cells. *Immunity* 36: 600–611.
14. Crites, T. J., L. Chen, and R. Varma. 2012. A TIRF microscopy technique for real-time, simultaneous imaging of the TCR and its associated signaling proteins. *J. Vis. Exp.* 61: pii 3892. Available at: http://www.jove.com/video/3892/a-tirf-microscopy-technique-for-real-time-simultaneous-imaging-tcr. doi:10.3791/3892.
15. Liu, D., Y. T. Bryceson, T. Meckel, G. Vasiliver-Shamis, M. L. Dustin, and E. O. Long. 2009. Integrin-dependent organization and bidirectional vesicular traffic at cytotoxic immune synapses. *Immunity* 31: 99–109.
16. Dustin, M. L., T. Starr, R. Varma, and V. K. Thomas. 2007. Supported planar bilayers for study of the immunological synapse. *Curr. Protoc. Immunol.* Chapter 18: Unit 18.13. doi:10.1002/0471142735.im1813s76
17. Axelrod, D. 2001. Total internal reflection fluorescence microscopy in cell biology. *Traffic* 2: 764–774.
18. Dustin, M. L., and J. A. Cooper. 2000. The immunological synapse and the actin cytoskeleton: molecular hardware for T cell signaling. *Nat. Immunol.* 1: 23–29.
19. Liu, D., T. Meckel, and E. O. Long. 2010. Distinct role of Rab27a in granule movement at the plasma membrane and in the cytosol of NK cells. *PLoS ONE* 5: e12870.
20. Biggs, M. J., M. C. Milone, L. C. Santos, A. Gondarenko, and S. J. Wind. 2011. High-resolution imaging of the immunological synapse and T-cell

receptor microclustering through microfabricated substrates. *J. R. Soc. Interface* 8: 1462–1471.
21. Rak, G. D., E. M. Mace, P. P. Banerjee, T. Svitkina, and J. S. Orange. 2011. Natural killer cell lytic granule secretion occurs through a pervasive actin network at the immune synapse. *PLoS Biol.* 9: e1001151.
22. Brown, A. C., I. M. Dobbie, J. M. Alakoskela, I. Davis, and D. M. Davis. 2012. Super-resolution imaging of remodeled synaptic actin reveals different synergies between NK cell receptors and integrins. *Blood* 120: 3729–3740.
23. Alpert, M. D., J. D. Harvey, W. A. Lauer, R. K. Reeves, M. Piatak, Jr., A. Carville, K. G. Mansfield, J. D. Lifson, W. Li, R. C. Desrosiers, et al. 2012. ADCC develops over time during persistent infection with live-attenuated SIV and is associated with complete protection against $SIV_{mac}251$ challenge. *PLoS Pathog.* 8: e1002890.
24. Zhang, F., Z. Wang, M. Lu, Y. Yonekubo, X. Liang, Y. Zhang, P. Wu, Y. Zhou, S. Grinstein, J. F. Hancock, and G. Du. 2014. Temporal production of the signaling lipid phosphatidic acid by phospholipase D_2 determines the output of extracellular signal-regulated kinase signaling in cancer cells. *Mol. Cell. Biol.* 34: 84–95.
25. Kim, E. S., R. S. Muller, and R. S. Hijab. 1992. Front-to-backside alignment using resist-patterned etch control and one etching step. *J. Microelectromech. Syst.* 1: 95–99.
26. Niklaus, F., P. Enoksson, E. Kälvesten, and G. Stemme. 2003. A method to maintain wafer alignment precision during adhesive wafer bonding. *Sens. Actuators A Phys.* 107: 273–278.
27. Kim, J. Y., J. Y. Baek, K. A. Lee, and S. H. Lee. 2005. Automatic aligning and bonding system of PDMS layer for the fabrication of 3d microfluidic channels. *Sens. Actuators A Phys.* 119: 593–598.
28. Howlader, M. M. R., A. Yamauchi, and T. Suga. 2011. Surface activation-based nanobonding and interconnection at room temperature. *J. Micromech. Microeng.* 21: 025009.
29. Lee, S. W., and S. S. Lee. 2007. Shrinkage ratio of PDMS and its alignment method for the wafer level process. *Microsyst. Technol.* 14: 205–208.
30. Mogi, K., and T. Fujii. 2013. A novel assembly technique with semi-automatic alignment for PDMS substrates. *Lab Chip* 13: 1044–1047.
31. Xia, Y., and G. M. Whitesides. 1998. Soft lithography. *Angew. Chem. Int. Ed.* 37: 550–575.
32. Zhang, K., C. K. Chou, X. Xia, M. C. Hung, and L. Qin. 2014. Block-cell-printing for live single-cell printing. *Proc. Natl. Acad. Sci. USA* 111: 2948–2953.
33. Zhang, Y., W. Zhang, and L. Qin. 2014. Mesenchymal-mode migration assay and antimetastatic drug screening with high-throughput microfluidic channel networks. *Angew. Chem. Int. Ed. Engl.* 53: 2344–2348.
34. Shankar, P. N., and M. D. Deshpande. 2000. Fluid mechanics in the driven cavity. *Annu. Rev. Fluid Mech.* 32: 93–136.
35. Le, D. V., B. C. Khoo, and J. Peraire. 2006. An immersed interface method for viscous incompressible flows involving rigid and flexible boundaries. *J. Comput. Phys.* 220: 109–138.
36. Grover, W. H., A. K. Bryan, M. Diez-Silva, S. Suresh, J. M. Higgins, and S. R. Manalis. 2011. Measuring single-cell density. *Proc. Natl. Acad. Sci. USA* 108: 10992–10996.
37. Mace, E. M., and J. S. Orange. 2014. Visualization of the immunological synapse by dual color time-gated stimulated emission depletion (STED) nanoscopy. *J. Vis. Exp.* 85: 51100. Available at: http://www.jove.com/video/51100/visualization-immunological-synapse-dual-color-time-gated-stimulated.
38. Marrack, P., A. C. N. Brown, S. Oddos, I. M. Dobbie, J.-M. Alakoskela, R. M. Parton, P. Eissmann, M. A. A. Neil, C. Dunsby, P. M. W. French, et al. 2012. Correction: Remodelling of cortical actin where lytic granules dock at natural killer cell immune synapses revealed by super-resolution microscopy. *PLoS Biol.* 10: 10.1371.
39. Stinchcombe, J. C., M. Salio, V. Cerundolo, D. Pende, M. Arico, and G. M. Griffiths. 2011. Centriole polarisation to the immunological synapse directs secretion from cytolytic cells of both the innate and adaptive immune systems. *BMC Biol.* 9: 45.
40. Jenkins, M. R., and G. M. Griffiths. 2010. The synapse and cytolytic machinery of cytotoxic T cells. *Curr. Opin. Immunol.* 22: 308–313.
41. Griffiths, G. M., A. Tsun, and J. C. Stinchcombe. 2010. The immunological synapse: a focal point for endocytosis and exocytosis. *J. Cell Biol.* 189: 399–406.
42. Bossi, G., C. Trambas, S. Booth, R. Clark, J. Stinchcombe, and G. M. Griffiths. 2002. The secretory synapse: the secrets of a serial killer. *Immunol. Rev.* 189: 152–160.
43. Stinchcombe, J. C., G. Bossi, S. Booth, and G. M. Griffiths. 2001. The immunological synapse of CTL contains a secretory domain and membrane bridges. *Immunity* 15: 751–761.
44. Costes, S. V., D. Daelemans, E. H. Cho, Z. Dobbin, G. Pavlakis, and S. Lockett. 2004. Automatic and quantitative measurement of protein-protein colocalization in live cells. *Biophys. J.* 86: 3993–4003.
45. Gatti, R., S. Belletti, G. Orlandini, O. Bussolati, V. Dall'Asta, and G. C. Gazzola. 1998. Comparison of annexin V and calcein-AM as early vital markers of apoptosis in adherent cells by confocal laser microscopy. *J. Histochem. Cytochem.* 46: 895–900.
46. Bussolati, O., S. Belletti, J. Uggeri, R. Gatti, G. Orlandini, V. Dall'Asta, and G. C. Gazzola. 1995. Characterization of apoptotic phenomena induced by treatment with L-asparaginase in NIH3T3 cells. *Exp. Cell Res.* 220: 283–291.
47. Weston, S. A., and C. R. Parish. 1990. New fluorescent dyes for lymphocyte migration studies. Analysis by flow cytometry and fluorescence microscopy. *J. Immunol. Methods* 133: 87–97.
48. Eccles, S. A., C. Box, and W. Court. 2005. Cell migration/invasion assays and their application in cancer drug discovery. *Biotechnol. Annu. Rev.* 11: 391–421.
49. Kummerow, C., E. C. Schwarz, B. Bufe, F. Zufall, M. Hoth, and B. Qu. 2014. A simple, economic, time-resolved killing assay. *Eur. J. Immunol.* 44: 1870–1872.
50. Vanherberghen, B., P. E. Olofsson, E. Forslund, M. Sternberg-Simon, M. A. Khorshidi, S. Pacouret, K. Guldevall, M. Enqvist, K. J. Malmberg, R. Mehr, and B. Önfelt. 2013. Classification of human natural killer cells based on migration behavior and cytotoxic response. *Blood* 121: 1326–1334.
51. Caramalho, I., M. Faroudi, E. Padovan, S. Müller, and S. Valitutti. 2009. Visualizing CTL/melanoma cell interactions: multiple hits must be delivered for tumour cell annihilation. *J. Cell. Mol. Med.* 13(9B): 3834–3846.
52. Angus, K. L., and G. M. Griffiths. 2013. Cell polarisation and the immunological synapse. *Curr. Opin. Cell Biol.* 25: 85–91.
53. Ritter, A. T., K. L. Angus, and G. M. Griffiths. 2013. The role of the cytoskeleton at the immunological synapse. *Immunol. Rev.* 256: 107–117.
54. Okazaki, T., S. Chikuma, Y. Iwai, S. Fagarasan, and T. Honjo. 2013. A rheostat for immune responses: the unique properties of PD-1 and their advantages for clinical application. *Nat. Immunol.* 14: 1212–1218.
55. Mentlik James, A., A. D. Cohen, and K. S. Campbell. 2013. Combination immune therapies to enhance anti-tumor responses by NK cells. *Front. Immunol.* 4: 481.
56. Long, E. O., H. S. Kim, D. Liu, M. E. Peterson, and S. Rajagopalan. 2013. Controlling natural killer cell responses: integration of signals for activation and inhibition. *Annu. Rev. Immunol.* 31: 227–258.
57. Abeyweera, T. P., E. Merino, and M. Huse. 2011. Inhibitory signaling blocks activating receptor clustering and induces cytoskeletal retraction in natural killer cells. *J. Cell Biol.* 192: 675–690.
58. Abeyweera, T. P., M. Kaissar, and M. Huse. 2013. Inhibitory receptor signaling destabilizes immunological synapse formation in primary NK cells. *Front. Immunol.* 4: 410.
59. Dustin, M. L., and E. O. Long. 2010. Cytotoxic immunological synapses. *Immunol. Rev.* 235: 24–34.